

Imprinting a Focused X-Ray Laser Beam to Measure Its Full Spatial Characteristics

J. Chalupský,^{1,*} P. Boháček,¹ T. Burian,¹ V. Hájková,¹ S. P. Hau-Riege,² P. A. Heimann,³ L. Juha,¹ M. Messerschmidt,³ S. P. Moeller,³ B. Nagler,³ M. Rowen,³ W. F. Schlotter,³ M. L. Swiggers,³ J. J. Turner,³ and J. Krzywinski³

¹*Institute of Physics, Academy of Sciences of the Czech Republic,
Na Slovance 2, 182 21 Prague, Czech Republic*

²*Lawrence Livermore National Laboratory, 7000 East Avenue, Livermore, California 94550, USA*

³*SLAC National Accelerator Laboratory, 2575 Sand Hill Road, Menlo Park, California 94025, USA*
(Received 9 October 2014; revised manuscript received 18 March 2015; published 14 July 2015)

The new generation of x-ray free-electron lasers opens up unique avenues for exploring matter under exotic and extreme conditions. Extensive spatial characterization of focused, typically (sub)micron-sized, laser beams is indispensable but, nevertheless, difficult to be accomplished due to excessive radiation intensities. Methods exist allowing indirect or semidirect focus characterization from a safe distance far from the focal point. Here we present a direct method of in-focus numerical phase recovery exploiting multishot desorption imprints in poly(methyl methacrylate). Shapes of the imprints serve as input data for the newly developed code PHARE (phase recovery), inspired by the iterative Gerchberg-Saxton algorithm. A procedure of dynamic input-output mixing guarantees that the algorithm always converges to a self-consistent paraxial Helmholtz equation solution, which is thereafter optimized for transverse spatial coherence. Very good agreement with single-shot ablation imprints in lead tungstate (PbWO₄) is found. The experiment is carried out at the Linac Coherent Light Source with a focused beam monochromatized at 800 eV. The results of the coherence optimization indicate that the act of monochromatization may have an effect on otherwise very good transverse coherence of free-electron laser beams.

DOI: 10.1103/PhysRevApplied.4.014004

I. INTRODUCTION

In the soft and hard x-ray spectral domain, routinely accessible by x-ray free-electron lasers (FELs) [1–5], the diffraction-limited spot size is intrinsically reduced due to very short wavelengths. This makes it possible to compress x-ray beams to (sub)micron foci [6,7] while achieving very high intensities. Therefore, direct focused beam characterization is not an easy task. Methods exist allowing remote focus characterization performed *in situ* in an indirect [8,9] or semidirect [10–12] manner. However, placement of the sensing element (e.g., an x-ray CCD or luminescence screen) directly at the focus is not safe due to excessive radiation intensities. Furthermore, very high transverse spatial resolution is required to sample the focal spot properly. Both requirements are usually met by placing the sensing element out of the high-intensity region where the spot size is sufficiently large. The intensity distribution and phase profile of the focal spot can be recovered numerically with the use of sophisticated backpropagation or phase-recovery algorithms. Semidirect methods [10–12], introducing a well-defined mask in the focal region, represent an important step towards the directness of such measurements. Nevertheless, making these measurements entirely direct would require placing the sensing element at

the focus, which is hardly achievable with standard detectors.

A few *ex situ* [13–16] and *in situ* [17] ablation imprint techniques have been proposed to overcome constraints connected with excessive intensities and resolution requirements at the focal point. Single-shot ablation imprints in various solid-state materials were exploited for direct *ex situ* characterization of focused soft x-ray laser beams. Ablation imprints in PMMA have been utilized to align a super-polished off-axis parabolic mirror and submicron focus [6] was achieved at the Free-electron Laser in Hamburg (FLASH). Consequently, a record peak intensity of approximately 10¹⁷ W/cm² was attained which enabled measurement of saturable absorption in aluminum at 13.5 nm [18] and spectroscopic investigation of warm dense aluminum plasma [19,20]. During the SXR (soft x-ray materials research) instrument commissioning, ablation imprints in lead tungstate (PbWO₄) served as a diagnostic tool for characterization of 800- and 1600-eV Linac Coherent Light Source (LCLS) beams [15]. Also, for a nonideal (non-Gaussian) beam, it has been experimentally proven that exact knowledge of the focused beam profile can markedly help with interpretation of laser-matter experimental results [21,22].

The original method of ablation imprints was first reported by Liu [23]. Silicon targets are used to characterize focused Gaussian beams in the visible and ultraviolet spectral range. This method is further extended to the

*Corresponding author.
chal@fzu.cz

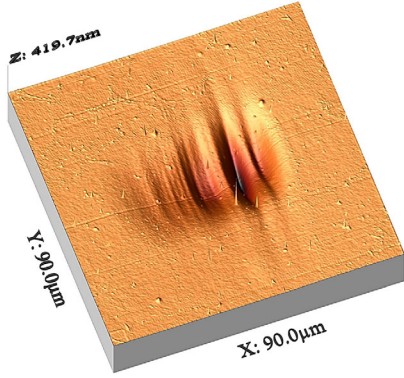


FIG. 1. A multishot (500 shots) desorption imprint in PMMA created by a focused LCLS beam monochromatized at 800 eV. The imprint is recorded out of focus ($z = 182$ mm), and the image is *ex situ* acquired by an AFM operated in the tapping mode. Owing to a high degree of spatial coherence in the horizontal direction (x), vertically oriented interference fringes, originating at the beam line x-ray optics, occur.

extreme ultraviolet and soft x-ray spectral domain [13,15] and to focused non-Gaussian beams [14,16]. Recently, it was experimentally demonstrated, but not yet published, that some targets can be used to characterize focused laser beams in the hard x-ray domain. Methods of ablation imprints were successfully utilized at the LCLS facility [4] tuned at 7.6 keV and SACLA (SPring-8 Angstrom Compact Free Electron Laser) facility [5] tuned at 12 keV. In the latter case, the beam characterization is performed for the purposes of interaction experiments aimed at radiation damage to x-ray optics induced by intense hard x rays [24]. Techniques of ablative imprints find applications not only in the short-wavelength spectral domain, e.g., in testing of focusing optics [25,26] and measurements of coherence properties of FEL beams [27], but also in the long-wavelength spectral region [28].

Initially, PMMA targets were solely used to characterize laser beams in the softer x-ray domain [13,14,16] ($\hbar\omega < 100$ eV), as the roughness of the ablated surface is significantly enhanced in the harder energy range. Nevertheless, it has been proposed that the so-called subthreshold desorption regime could be used for multishot beam imprinting [29,30]. As shown in Fig. 1, multishot desorption imprints in PMMA are usually smooth and do not indicate any threshold behavior; hence, desorption imprints are not truncated, which is typical for ablation imprints. The above phenomena allow us to discern fine structures of the focused beam over an extended wavelength range provided that the beam-pointing stability is satisfactory. In accord with the phenomenological model [29], the desorbed crater profile is proportional to the incident fluence profile and thereby to the square of the electrical field modulus. Consequently, fluence profiles are measurable, for example, by means of atomic force microscopy with ultrahigh spatial resolution.

The “measured” field moduli serve as input data for the phase-recovery algorithm reported in this paper. Utilization of desorption imprints represents an approach which enables full and direct spatial characterization of focused laser beams. Therefore, it considerably extends the capabilities of current (ablative) imprinting methods.

The paper is organized as follows: In Sec. II, we describe the experimental layout, the procedure of target irradiation, and the technique of microscopy analysis. Section III details the phase-recovery algorithm, especially preprocessing methods and the procedure of iterative phase retrieval. Section IV deals with the postprocessing procedure of coherence optimization which evaluates and incorporates partial coherence into the phase-recovery result. Section V is devoted to a discussion of the results and a comparison with single-shot ablation imprints in lead tungstate. Furthermore, an effect of monochromatization on otherwise very good transverse coherence of FEL sources is discussed here. Section VI concludes the paper. Appendixes A–C summarize the mathematical background of the coherence optimization technique employed in the PHARE code.

II. EXPERIMENT

All experimental data are collected during the commissioning phase of the SXR/LCLS instrument [31–33] with use of a varied-line-spacing (VLS) grating monochromator [31]. The FEL beam is first focused in the vertical direction with the use of a grazing incidence spherical mirror ($M1$) to an exit slit of variable width. The role of the exit slit is to spectrally select a desired part of the otherwise much broader FEL spectrum which is vertically projected onto the slit plane by the VLS grating and the spherical mirror. The reflective VLS grating and the exit slit are located 0.3 and 7.8 m downstream from the spherical mirror, respectively. Vertical ($M2$) and horizontal ($M3$) focusing mirrors of an adaptive Kirkpatrick-Baez (KB) optical system are positioned 4.5 and 5 m downstream from the monochromator’s exit slit, respectively. This optical system allows for independent and adjustable focusing in both the horizontal and vertical directions. The position of the focus is changeable; however, its default location is 1.5 m downstream from the last (horizontal) KB mirror. All optical surfaces are thin B_4C layers coated on superpolished substrates [34].

A VLS grating with a center line density of 100 l/mm is used to monochromatize the LCLS beam to 800 eV and to eliminate higher harmonics. The LCLS beam is incident upon the grating under a grazing angle of 19.5 mrad, and the first negative diffraction order is used. The vertical opening of the exit slit is 30 μm , which is approximately twice less than the vertical second central moment (SCM) width of the dispersed spectrum at this location and photon energy. PMMA samples are positioned approximately 150 cm downstream from the last horizontal KB mirror (at the expected focus location) and oriented

perpendicularly to the incident laser beam. All irradiated samples are mounted on a target holder which is actuated by a three-axis translational manipulator. Exposures are conducted in a vacuum chamber allowing longitudinal translation over a range of 240 mm.

During the experiment, several multishot desorption imprints at different longitudinal positions are recorded on the PMMA surface in order to probe the focus and its surroundings. Hundreds of shots (100, 300, and 500) are accumulated at the same spot to attain a reasonable imprint contrast. Since the damage mechanism must remain in the linear desorption regime (i.e., the peak fluence must not overshoot the single-shot ablation threshold), a nitrogen-filled gas attenuator is used to reduce the pulse energy down to 0.1% of the maximum available pulse energy. Through-focus scans are repeated at several different attenuation levels (full power, 10%, 1%, and 0.1%) in order to stay below the single-shot ablation threshold at all longitudinal positions, i.e., at the focus and in out-of-focus regions. The shapes of the imprints are *ex situ* investigated by atomic force microscopy (AFM). Ablated imprints and imprints evincing a nonlinear response due to an excessive accumulated dose are excluded from further analysis.

All measurements are carried out in the tapping mode with use of a Dimension 3100 scanning probe microscope driven by a NanoScope IV controller (Veeco, USA). The acquisition of each image with the use of this particular device requires approximately 30 min. However, the capabilities of new microscopy devices, especially of white-light interferometers, continuously improve. This makes it possible to acquire high-resolution three-dimensional images within a few seconds. The utilization of such devices has a prospective *in situ* application in future beam-characterization methods exploiting ablation and desorption imprints.

III. PHASE-RECOVERY ALGORITHM

Our phase-recovery code (PHARE) is written by using the Interactive Data Language (IDL) and comprises of three major parts. In the first preprocessing part, beam profile (AFM) data are loaded and appropriately refined by filters. It follows from the momentum-conservation law that the centroid of transverse intensity distribution must follow a straight line as the laser pulse propagates in free space. Therefore, centroids of all measured intensity profiles must be shifted to the center of each image, i.e., positioned at the longitudinal z axis (optical axis). It should be also noted that all AFM data need to be acquired under the same sample-to-microscope orientation; otherwise, the coordinate system becomes undefined. The modified intensity data are normalized in the sense of the L^2 norm. This requirement arises from the energy-conservation law, which must be met as the laser pulse propagates in free space. From here, it follows that the integral (volume) below the normalized intensity profile is constant with a

longitudinal z position. Finally, electrical field amplitudes $|E_n^M|$ are calculated as a square root of normalized intensity distributions. Figure 2(a) depicts the electrical field profiles assigned to their corresponding z positions, which serve as input data for the main processor.

The main body of the code solves the phase problem in the Fresnel (paraxial) approximation. The code works similarly to the Gerchberg-Saxton (GS) [35–37] and related algorithms [38], but, unlike the GS algorithm, PHARE is naturally constrained by the measured data, and Fresnel propagation is used to retrieve the complex field curvature. To illustrate this, a schematic layout of the phase-recovery algorithm, applied to a sequence of three intensity measurements, is shown in Fig. 3(a). The field propagation between two neighboring positions n and $m = n \pm 1$ is realized by a convolution of the initial field $E_n = |E_n| \exp(i\varphi_n) = E(\mathbf{\rho}, z_n)$ with the Fresnel propagation kernel $\exp[ik|\mathbf{\rho}|^2/(2\zeta_{nm})]$. Here $\mathbf{\rho}$ denotes the transverse coordinate vector, $\zeta_{nm} = z_m - z_n$ is the mutual longitudinal distance between the initial (z_n) and final (z_m) position, k is the angular wave number, and $|E_n|$ and φ_n are an updated (recovered) modulus and phase, respectively, at the initial position z_n . The Fresnel propagation can be more conveniently performed in the Fourier domain as the convolution changes to a simple multiplication:

$$\hat{E}^T(\mathbf{\kappa}, z_m) = \hat{E}(\mathbf{\kappa}, z_n) \exp\left(-\frac{i\zeta_{nm}}{2k} \mathbf{\kappa}^2\right), \quad (1)$$

where $\mathbf{\kappa}$ is the transverse coordinate vector in k space and the wedge symbol stands for the Fourier transform. From the inverse Fourier transform, a temporary complex electrical field is obtained and split into the modulus and phase: $E_m^T = |E_m^T| \exp(i\varphi_m)$.

In early iteration loops, the input fields, which are subject to propagation, are constructed from the corresponding measured field moduli and updated (recovered) phases. Nevertheless, due to possible inaccuracies in the measurement, the resultant electrical field may still deviate from the self-consistent paraxial Helmholtz equation solution despite the algorithmic convergence tending to a stagnation point [see Fig. 3(b)]. Hence, in later iteration loops, a dynamic input-output mixing subroutine is implemented in order to remove the measured field moduli from the recovery process and to replace them smoothly by the recovered ones. For this purpose, the electrical fields E_n , entering the j th phase retrieval loop, are always constructed as a linear combination of the measured (M) and temporary (T) field modulus: $E_n = (\alpha_j |E_n^M| + \beta_j |E_n^T|) \exp(i\varphi_n)$. Here α_j and β_j are dynamic scaling factors dependent on the iteration loop number j , as plotted in Fig. 3(b). These scaling factors obey a condition $\alpha_j + \beta_j = 1$ for all iteration loops. As depicted in Fig. 3(b), no input-output mixing is imposed in the first 40 iterations, and the convergence quickly tends to a stagnation point in terms

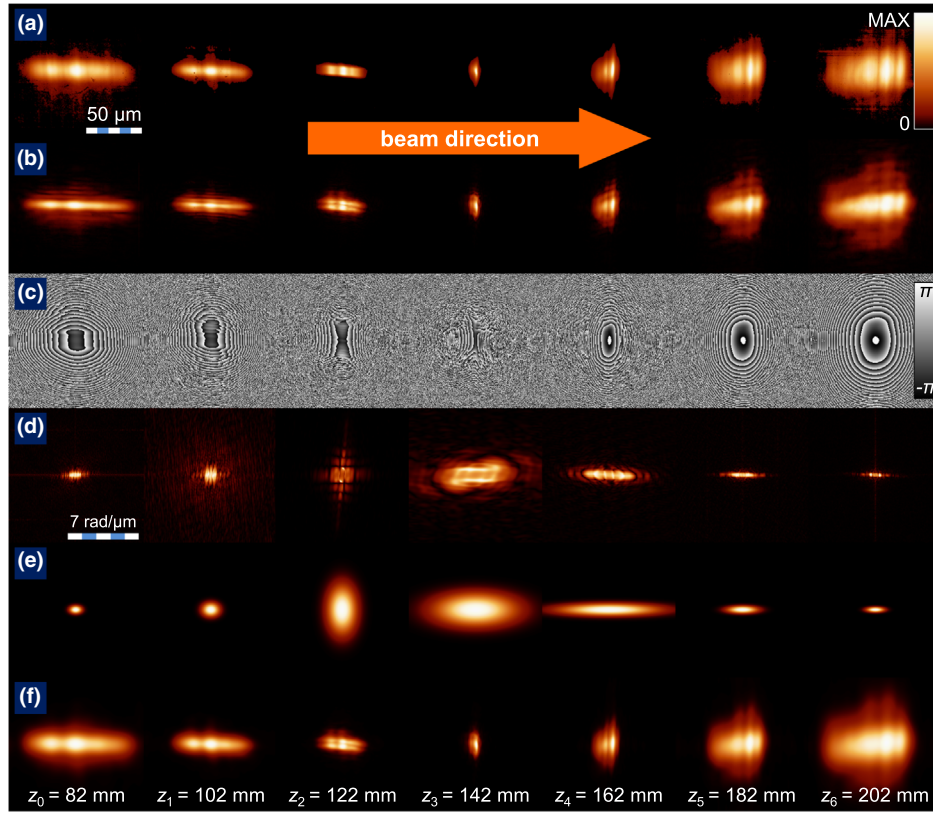


FIG. 2. A visualization of input and output data generated by the PHARE code. Row (a) depicts measured electrical field moduli, rows (b) and (c) show recovered (fully coherent and self-consistent) field amplitudes and phases modulo 2π , rows (d) and (e) visualize the recovered $g_S(\mathbf{k}, z_n)$ function and the fit of the astigmatic Gaussian Schell model, and row (f) displays coherence optimized field amplitudes. All images, except for rows (d) and (e), are in the same scale, and each column is assigned a corresponding z position. Images in rows (d) and (e) are in the reciprocal space and in the same scale. Both color scales for amplitude and phase are linear.

of the total χ squared (total sum of squared differences between corresponding measured and recovered field moduli). Within the next 40 iterations, the α factor linearly drops from 1 to 0, whereas the β factor rises from 0 to 1, which leads to a dynamic input-output mixing. Consequently, the measured field amplitudes are entirely and smoothly removed from the calculation. No change in the total χ squared within the last 20 iterations confirms a self-consistent propagation of the resultant field, whence it follows that a solution of the paraxial Helmholtz equation is found. Recovered field moduli and phases are depicted in Figs. 2(b) and 2(c), and a complete recorded code run is shown in Video 1.

IV. COHERENCE OPTIMIZATION

Since the retrieved electrical field must be considered as fully transversally coherent, some additional features may appear in the recovered beam profiles and the divergence may be lower than expected. Evidently, by comparing Figs. 2(a) and 2(b), it can be seen that the recovered beam divergence is noticeably reduced in the vertical direction, which indicates possible coherence issues. Therefore, the

resultant data need to be optimized for the partial coherence which is carried out in the third postprocessing part of the code. For this purpose, the so-called Schell model [39–42] is employed. It is a beneficial property of this model that the modulus of the complex degree of transverse coherence (at equal time) can be revealed numerically from the measured and recovered intensity data. As shown in Appendixes A and B, the Fourier transform of the partially coherent intensity profile at an arbitrary z position can be expressed as

$$\begin{aligned} \hat{I}^{\text{pc}}(\mathbf{k}, z) &= \hat{I}^{\text{fc}}(\mathbf{k}, z) g \left[\frac{\mathbf{k}}{k} (z - z_S), z_S \right] \\ &= \hat{I}^{\text{fc}}(\mathbf{k}, z) g_S(\mathbf{k}, z), \end{aligned} \quad (2)$$

where $\hat{I}^{\text{pc}}(\mathbf{k}, z)$ and $\hat{I}^{\text{fc}}(\mathbf{k}, z)$ are the Fourier-transformed partially and fully coherent intensities, respectively, and $g(\bullet, z_S)$ is the Schell approach to the complex degree of coherence at the secondary Schell-model source position z_S . Provided that the recovered and measured electrical fields correspond, respectively, to the fully coherent and partially coherent case of the studied beam,

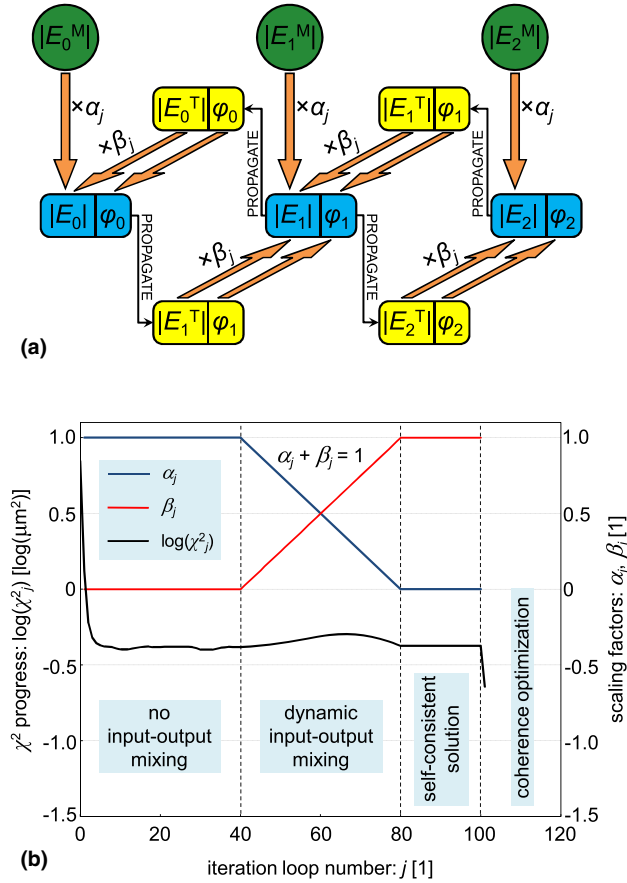
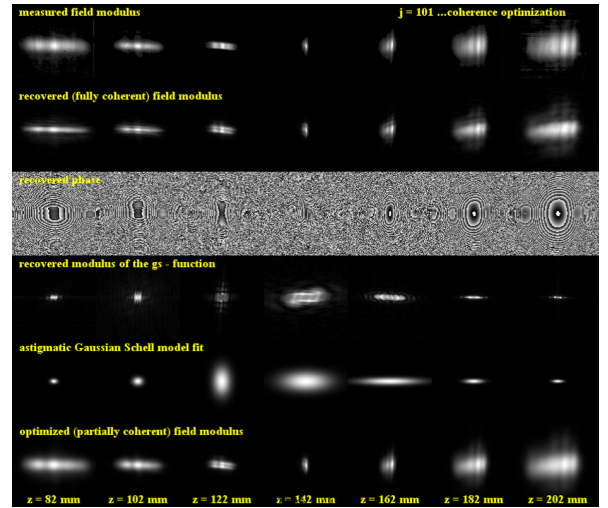


FIG. 3. A sketch of basic operations performed by the PHARE code. (a) An illustrative flow chart depicting the j th iteration loop of the phase-retrieval algorithm applied to three consecutive intensity measurements. This layout can be extended to an arbitrary number of positions. Green circles stand for the measured field moduli $|E_n^M|$, yellow rectangles represent temporary electrical fields $|E_n^T| \exp(i\varphi_n)$, and blue rectangles contain the recovered electrical fields $|E_n| \exp(i\varphi_n)$ consisting of the modulus $|E_n|$ and phase φ_n . The recovered field modulus is constructed as a linear combination of the corresponding measured and temporary modulus $\alpha_j |E_n^M| + \beta_j |E_n^T|$. This combination is dynamically scaled by factors α_j and β_j plotted in (b) with respect to the iteration loop number. (b) also shows the progress of the total χ squared and clearly displays the particular phases of the algorithm, i.e., no I-O mixing (drop in χ^2 followed by stagnation), dynamic I-O mixing (local χ^2 increase followed by a drop), self-consistent solution (no change in χ^2), and coherence optimization (drop in χ^2).

i.e., $I^{\text{fc}}(\mathbf{\rho}, z_n) \sim |E(\mathbf{\rho}, z_n)|^2$ and $I^{\text{pc}}(\mathbf{\rho}, z_n) \sim |E^M(\mathbf{\rho}, z_n)|^2$, we can recover the modulus of the $g_S(\mathbf{\kappa}, z_n)$ function to some reasonable accuracy, as justified in Appendix C and depicted in Fig. 2(d).

In the present study, an astigmatic Gaussian Schell model of the following form (see Appendix C):

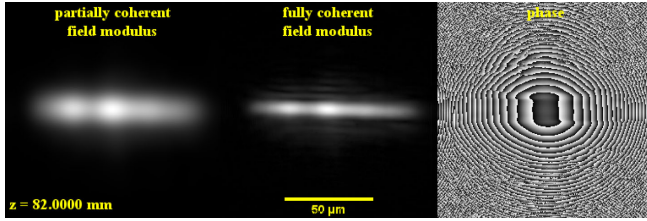
$$g_S(\mathbf{\kappa}, z) = \exp \left[-\frac{(z - z_{Sx})^2}{2k^2 \sigma_{Sx}^2} \kappa_x^2 - \frac{(z - z_{Sy})^2}{2k^2 \sigma_{Sy}^2} \kappa_y^2 \right], \quad (3)$$



VIDEO 1. A complete recorded run of the PHARE code.

is globally fitted to the coherence data [see Fig. 2(e)] in order to determine the coherence widths σ_{Sx} and σ_{Sy} at the positions z_{Sx} and z_{Sy} of the respective horizontal (x) and vertical (y) Schell-model sources. Based on the aforementioned results, coherence optimized intensity profiles can be retrieved at any longitudinal position with the use of Eqs. (1)–(3). This is illustrated by Video 2, which shows the coherence optimized field modulus, fully coherent field modulus, and phase of the beam as it propagates in the measurement range. Evidently, the Schell model can be very helpful in solving the coherence phenomena being in general enormously computationally difficult. However, it should be kept in mind that the Schell model and its astigmatic Gaussian approximation still represent a two-dimensional approach to an otherwise four-dimensional complex degree of coherence. This indispensably brings certain limitations on accuracy.

In contrary to the fully coherent results in Fig. 2(b), the coherence optimized results in Fig. 2(f) closely resemble the measured data displayed in Fig. 2(a). The legitimacy of these results is also indicated by a significant reduction of the total χ squared, as shown in Fig. 3(b). In accord with Eq. (C6), applicable to Gaussian Schell-model beams, the degree of transverse coherence in the horizontal direction is found to be $\xi_x = 84\%$. This result is in very good agreement with double-slit measurements [43] performed at the same LCLS instrument. Nevertheless, the degree of transverse coherence in the vertical direction is as low as $\xi_y = 38\%$, albeit a similar value as in the horizontal direction is expected. For this result, there are at least two possible explanations, both connected with the presence of the monochromator having its dispersion axis oriented vertically. First, due to the central wavelength jitter, the beam-pointing instability in the vertical direction may be increased. Consequently, the accumulated imprint may appear broader. The second explanation resides in the



VIDEO 2. A simulation of the recovered beam showing the partially coherent field modulus, fully coherent field modulus, and phase as the beam propagates in the measurement range.

poor temporal (spectral) coherence of FEL sources, which, upon monochromatization, may negatively influence otherwise very good transverse coherence in the direction of dispersion. This is in more detail discussed in the next section.

V. DISCUSSION

For the purposes of comparison, several single-shot ablation imprints are recorded in lead tungstate (PbWO_4) under the same beam conditions as in PMMA. Despite the different nature of the damage process in ionic crystals and different irradiation regimes (single-shot ablation vs multi-shot desorption), the shapes of these ablative imprints, their orientation, and the appearance of fringes show an excellent consistency with the coherence optimized field profiles numerically recovered at the corresponding positions (see Fig. 4).

The consistency of the results partly disproves the first argument for the reduced degree of transverse coherence in the vertical direction, since single-shot imprints are not sensitive to the pointing jitter. In this particular case, the shot-to-shot variation of laser beam parameters appears to have a minor effect on the phase-recovery result obtained from averaged electrical field profiles. The consistency of both results could be ascribed to a very good beam stability and to the self-consistency of the numerical solution substantially reducing its possible ambiguity.

From the ablative imprints in PbWO_4 (z scan), basic beam propagation parameters can be estimated if an astigmatic Gaussian beam is assumed [15]. Figure 5 compares effective caustic curves [14] generated by PHARE with PbWO_4 results. Despite the beam being aberrated and non-Gaussian, these two distinct methods show a very good agreement in their results and mutually confirm their correctness.

The transverse coherence issue, raised by the coherence optimized results of the PHARE code, has to be discussed in a broader context. The coherence properties of FEL beams generated in undulators largely follow from the nature of the self-amplified spontaneous emission process starting from the shot noise. The degree of transverse coherence can reach very high values close to unity, whereas temporal coherence is obviously low. A coherence time of 0.55 fs (SCM) is measured at the Linac Coherent Light Source tuned at 780 eV [43]. Comparing the coherence time with the pulse duration of 127 fs (SCM), one may expect very low temporal coherence, which is a consequence of the very complex modal structure of the FEL wave field. A typical power spectrum of single FEL pulses reveals many narrow and separate peaks representing mutually incoherent longitudinal modes. These modes originate in the shot noise and are independently amplified at slightly different frequencies. We can illustrate their presence by a demagnified image of the exit slit formed by KB optics. Figure 6(a) depicts an exit-slit image (transverse intensity profile) recovered with the use of the PHARE code, and Fig. 6(b) shows the corresponding single-shot ablative imprint in lead tungstate (PbWO_4). Three separate modes are clearly discernible in both images; the remaining part of the spectrum is clipped off by the exit slit.

The monochromatized FEL wave field may considerably differ from the original one in many aspects, including the beam shape and transverse coherence. The wave field in the horizontal direction (perpendicular to the dispersion direction) remains almost unaffected by the act of monochromatization, which indicates an invariability of the degree of

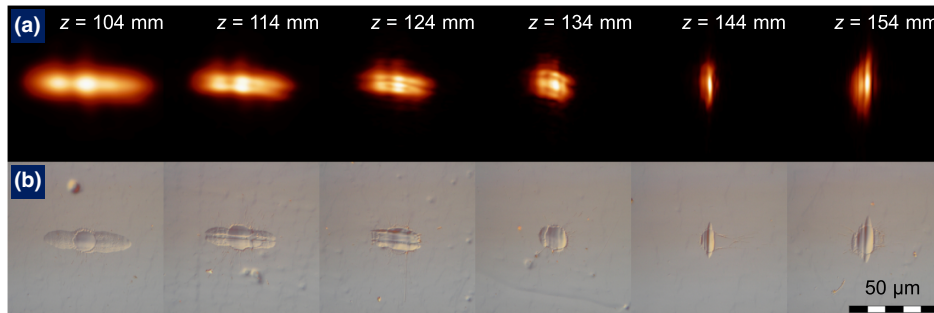


FIG. 4. A comparison between the recovered coherence optimized field amplitudes and single-shot ablative imprints in lead tungstate. The recovered electrical field (a) is propagated to the corresponding z positions with the use of the Fresnel propagation and thereafter optimized for the partial coherence. PbWO_4 imprints (b) are examined by using a Nomarski differential interference contrast microscope. An apparent difference in sizes, but not in shapes, is caused by the threshold nature of the ablation process leading to truncation of the imprinted beam profile at a certain threshold fluence level. All images are in the same scale.

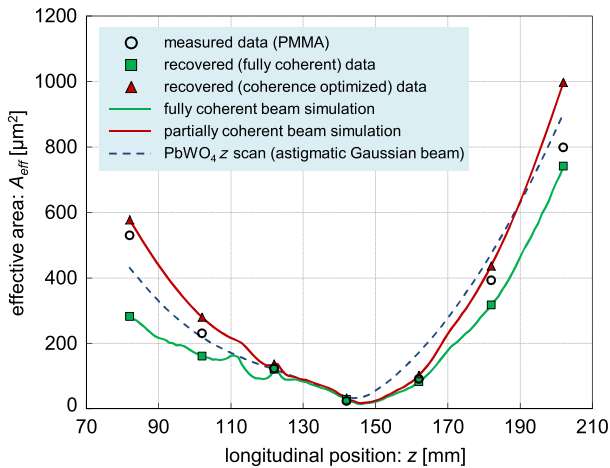


FIG. 5. A plot depicting the z dependence of the effective area of the beam. Plotted values represent the measured data (black open circles), recovered fully coherent data (green squares), and coherence optimized data (red triangles). The solid green and red lines stand for the simulated fully coherent and coherence optimized beam, respectively, whereas the dashed blue line represents the effective caustic curve evaluated from the PbWO_4 z scan in an astigmatic Gaussian beam approach.

transverse coherence in this direction. This was verified by the phase-recovery measurement, since the determined value of the degree of transverse coherence ($\xi_x = 84\%$) is in a very good agreement with the double-slit measurement (75%) done with the nonmonochromatized beam of comparable photon energy [43]. However, a quite different situation occurs in the vertical direction, i.e., in the direction of dispersion. The vertical beam profile at the exit-slit position represents the power spectrum of the corresponding FEL pulse. Hence, fluctuations and correlations in the FEL spectrum should have an effect on statistical properties of the wave field in the vertical direction. In other words, being transposed by the monochromator from the spectral to the spatial domain, the power spectrum and complex degree of spectral coherence

should correspond to the intensity profile and complex degree of transverse coherence at the exit slit, respectively. Since the coherence time is much shorter than the pulse duration, we can treat this FEL radiation nearly as a stationary random process. Therefore, we can claim that the spectral width, being inversely proportional to the coherence time [44], is much greater than the spectral coherence width, being inversely proportional to the pulse duration. Upon monochromatization, the spectral width and spectral coherence width are, via the grating equation, transformed to the transverse (vertical) beam width and coherence width at the position of the exit slit, respectively. If we compare the resultant SCM coherence width (approximately $0.3 \mu\text{m}$) with the SCM slit width (approximately $8.7 \mu\text{m}$ for uniform illumination), then, according to Eq. (C6), we must conclude that the degree of transverse coherence is very small ($\xi_y \sim 2\%$). This is, however, what we observe neither in PHARE simulations nor in PbWO_4 measurements. The origin of this discrepancy resides in the resolving power of the monochromator, which is not taken into account. A resolving power of 3000 is measured at the SXR instrument [31]; hence, the SCM width of the resolution function at the exit slit is approximately $6.3 \mu\text{m}$ for 800-eV photons and the first negative diffraction order. The power spectrum (or the transverse beam profile in the vertical direction) as well as the complex degree of spectral coherence (or the complex degree of coherence in the vertical direction) must be convolved with the monochromator's resolution function (typically of a Gaussian shape) in order to get the real profiles. The transverse coherence width of the convolved complex degree of coherence then approximately equals the width of the resolution function (approximately $6.3 \mu\text{m}$), since its “nonconvolved” value (approximately $0.3 \mu\text{m}$) is negligibly small. Inserting this value and the SCM slit width into Eq. (C6), we get $\xi_y \sim 34\%$, which is in a very good agreement with the degree of transverse coherence evaluated by the PHARE code ($\xi_y = 38\%$).

VI. CONCLUSIONS

In summary, a focused soft x-ray laser beam, monochromatized at 800 eV, is characterized directly at the focal point and its surroundings with the use of multishot desorption imprints in PMMA. The shapes of the imprints serve as input data for the PHARE code, which recovers a self-consistent solution of the paraxial Helmholtz equation. The Schell model is used to optimize the fully coherent result for partial coherence. The coherence optimized results show a very good agreement with single-shot ablation imprints in lead tungstate created under the same beam conditions. It is also found that the act of monochromatization may have a negative effect on otherwise very good transverse coherence of FEL beams. The imprinting methods, discussed here, show the capability to explore focused x-ray laser beams directly and,

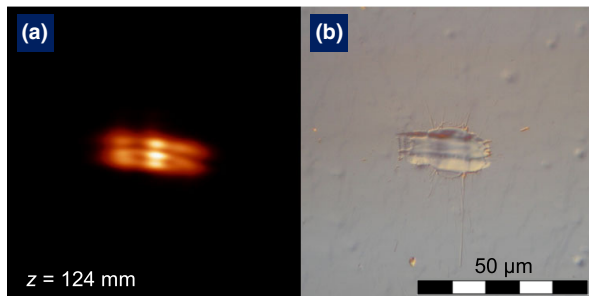


FIG. 6. An image of the monochromator's exit slit projected by the Kirkpatrick-Baez focusing optics. (a) Coherence optimized intensity profile recovered by the PHARE code at the longitudinal position $z = 124 \text{ mm}$. (b) A single-shot ablative imprint in lead tungstate (PbWO_4) created at the same longitudinal position.

therefore, to add to the ensemble of tools available for rigorous focused x-ray laser beam characterization, a critical step for the future of x-ray sources such as FELs.

ACKNOWLEDGMENTS

The Czech authors gratefully acknowledge funding from the Czech Ministry of Education via Grants No. ME10046 and No. LH14072 supporting the Czech-U.S. scientific cooperation within the funding scheme KONTAKT. J. C. thanks the Academy of Sciences of the Czech Republic for postdoctoral financial support. Use of the Linac Coherent Light Source (LCLS), SLAC National Accelerator Laboratory, is supported by the U.S. Department of Energy, Office of Science, Office of Basic Energy Sciences under Contract No. DE-AC02-76SF00515. The SXR Instrument is funded by a consortium whose membership includes the LCLS, Stanford University through the Stanford Institute for Materials Energy Sciences (SIMES), Lawrence Berkeley National Laboratory (LBNL), University of Hamburg through the BMBF priority program FSP 301, and the Center for Free Electron Laser Science (CFEL). Part of this work was performed under the auspices of the U.S. Department of Energy by Lawrence Livermore National Laboratory under Contract DE-AC52-07NA27344.

APPENDIX A: FRESNEL PROPAGATION OF PARTIALLY COHERENT WAVE FIELDS

The propagation of monochromatic partially coherent beams can be conveniently described in terms of the mutual optical intensity $J(\mathbf{r}_1, \mathbf{r}_2)$ [41], which is sometimes referred to as the “equal-time correlation function” [40]. It can be defined as

$$J(\mathbf{r}_1, \mathbf{r}_2) = \Gamma(\mathbf{r}_1, \mathbf{r}_2, 0) = \langle E^*(\mathbf{r}_1, t)E(\mathbf{r}_2, t) \rangle_{\text{ensemble}}. \quad (\text{A1})$$

where $\Gamma(\mathbf{r}_1, \mathbf{r}_2, 0)$ is the equal-time mutual coherence function, E is the scalar electrical field, and the angular brackets denote ensemble averaging. In fact, the mutual optical intensity (MOI) describes binary correlations of the electrical field at two different positions \mathbf{r}_1 and \mathbf{r}_2 and at equal time t . In the Fresnel approximation, the mutual optical intensity can be propagated along the optical axis of the beam by solving the following integral:

$$\begin{aligned} J(\boldsymbol{\rho}_1, \boldsymbol{\rho}_2, z) &= \frac{k^2}{4\pi^2\zeta^2} \iint_{R^2} \iint_{R^2} J(\boldsymbol{\rho}'_1, \boldsymbol{\rho}'_2, z') \\ &\times \exp\left[-\frac{ik}{2\zeta} |\boldsymbol{\rho}_1 - \boldsymbol{\rho}'_1|^2\right] \\ &\times \exp\left[\frac{ik}{2\zeta} |\boldsymbol{\rho}_2 - \boldsymbol{\rho}'_2|^2\right] d^2\rho'_1 d^2\rho'_2. \end{aligned} \quad (\text{A2})$$

Here $\boldsymbol{\rho}_1$, $\boldsymbol{\rho}_2$, $\boldsymbol{\rho}'_1$, and $\boldsymbol{\rho}'_2$ denote transverse coordinates at the final (nonprimed) and initial (primed) transverse plane, and k is the angular wave number. The planes are mutually separated by $\zeta = z - z'$. The intensity profile at the final plane is given by MOI at one point $\boldsymbol{\rho}_1 = \boldsymbol{\rho}_2 = \boldsymbol{\rho}$; hence, it can be expressed as

$$\begin{aligned} I(\boldsymbol{\rho}, z) \propto J(\boldsymbol{\rho}, \boldsymbol{\rho}, z) &= \frac{k^2}{4\pi^2\zeta^2} \iint_{R^2} \iint_{R^2} \tilde{J}_\zeta(\boldsymbol{\rho}'_1, \boldsymbol{\rho}'_2, z') \\ &\times \exp\left[\frac{ik}{\zeta} \boldsymbol{\rho} \cdot (\boldsymbol{\rho}'_1 - \boldsymbol{\rho}'_2)\right] d^2\rho'_1 d^2\rho'_2, \end{aligned} \quad (\text{A3})$$

where the MOI with the tilde is for the purposes of further facilitation defined as

$$\tilde{J}_\zeta(\boldsymbol{\rho}'_1, \boldsymbol{\rho}'_2, z') = J(\boldsymbol{\rho}'_1, \boldsymbol{\rho}'_2, z') \exp\left[\frac{ik}{2\zeta} (|\boldsymbol{\rho}'_2|^2 - |\boldsymbol{\rho}'_1|^2)\right]. \quad (\text{A4})$$

The Fourier-transformed intensity then reads

$$\begin{aligned} \hat{I}(\boldsymbol{\kappa}, z) &= \iint_{R^2} I(\boldsymbol{\rho}, z) \exp(-i\boldsymbol{\kappa} \cdot \boldsymbol{\rho}) d^2\rho \\ &\propto \frac{k^2}{4\pi^2\zeta^2} \iint_{R^2} \iint_{R^2} \iint_{R^2} \tilde{J}_\zeta(\boldsymbol{\rho}'_1, \boldsymbol{\rho}'_2, z') \\ &\times \exp\left[-\frac{ik}{\zeta} \boldsymbol{\rho} \cdot \left(\boldsymbol{\kappa} \frac{\zeta}{k} + \boldsymbol{\rho}'_2 - \boldsymbol{\rho}'_1\right)\right] \\ &\times d^2\rho'_1 d^2\rho'_2 d^2\rho. \end{aligned} \quad (\text{A5})$$

The integral of the exponential function results in a δ function:

$$\begin{aligned} \iint_{R^2} \exp\left[-\frac{ik}{\zeta} \boldsymbol{\rho} \cdot \left(\boldsymbol{\kappa} \frac{\zeta}{k} + \boldsymbol{\rho}'_2 - \boldsymbol{\rho}'_1\right)\right] d^2\rho \\ = \frac{4\pi^2\zeta^2}{k^2} \delta\left(\boldsymbol{\kappa} \frac{\zeta}{k} + \boldsymbol{\rho}'_2 - \boldsymbol{\rho}'_1\right), \end{aligned} \quad (\text{A6})$$

whence it follows that the Fourier-transformed intensity obtains a very simple form:

$$\hat{I}(\boldsymbol{\kappa}, z) \propto \iint_{R^2} \tilde{J}_\zeta\left(\boldsymbol{\rho}', \boldsymbol{\rho}' - \boldsymbol{\kappa} \frac{\zeta}{k}, z'\right) d^2\rho'. \quad (\text{A7})$$

APPENDIX B: THE SCHELL MODEL

The generalized Schell model [39–42] describes to a good approximation coherence properties of many laser sources. In the frame of this model, the transverse intensity distribution at the position $z' = z_S$ of the secondary Schell-model source has always the same shape irrespective of the coherence state. In other words, the beam profile of the secondary Schell-model source is independent of the degree of transverse coherence, whether it be full, partial, or none (incoherent). Therefore, partially coherent Schell-model beams are usually propagated from the source position where the initial mutual optical intensity can be factorized as

$$\tilde{J}_\zeta^{\text{pc}}(\boldsymbol{\rho}'_1, \boldsymbol{\rho}'_2, z_S) = \tilde{J}_\zeta^{\text{fc}}(\boldsymbol{\rho}'_1, \boldsymbol{\rho}'_2, z_S)g(\boldsymbol{\rho}'_1 - \boldsymbol{\rho}'_2, z_S). \quad (\text{B1})$$

Here J_ζ^{pc} and J_ζ^{fc} with tildes are partially and fully coherent mutual optical intensities, respectively, and $g(\boldsymbol{\rho}'_1 - \boldsymbol{\rho}'_2, z_S)$ is the Schell approach to the complex degree of coherence at the secondary Schell-model source position. By substituting the partially coherent MOI from Eq. (B1) to Eq. (A7), we obtain a factorized expression for the Fourier-transformed partially coherent intensity at an arbitrary z position:

$$\begin{aligned} \hat{I}^{\text{pc}}(\mathbf{k}, z) &= \hat{I}^{\text{fc}}(\mathbf{k}, z)g\left[\frac{\mathbf{k}}{k}(z - z_S), z_S\right] \\ &= \hat{I}^{\text{fc}}(\mathbf{k}, z)g_S(\mathbf{k}, z), \end{aligned} \quad (\text{B2})$$

where the Fourier-transformed fully coherent intensity reads

$$\hat{I}^{\text{fc}}(\mathbf{k}, z) \propto \iint_{R^2} \tilde{J}_\zeta^{\text{fc}}\left[\boldsymbol{\rho}', \boldsymbol{\rho}' - \frac{\mathbf{k}}{k}(z - z_S), z_S\right] d^2\rho'. \quad (\text{B3})$$

Equation (B2) means that for any point z the partially coherent intensity distribution $I^{\text{pc}}(\boldsymbol{\rho}, z)$ is given by a convolution of the fully coherent intensity distribution $I^{\text{fc}}(\boldsymbol{\rho}, z)$ with an inverse Fourier image of the function $g_S(\mathbf{k}, z)$. It naturally follows from Eq. (B2) that fully and partially coherent intensity profiles must be identical at the secondary Schell-model source position, since $g_S(\mathbf{k}, z_S) = 1$. In compliance with our expectations of a fully coherent laser beam, the intensity profiles $I^{\text{pc}}(\boldsymbol{\rho}, z)$ and $I^{\text{fc}}(\boldsymbol{\rho}, z)$ will be identical in the whole space, since $g_S(\mathbf{k}, z) = 1$ for all z positions. In the case of a fully coherent beam, the inverse Fourier image of $g_S(\mathbf{k}, z)$ is the δ function acting as the identity in the convolution, whereas, in the case of a partially coherent beam, the inverse Fourier image of $g_S(\mathbf{k}, z)$ has nonzero width, which is a cause of increased beam divergence.

APPENDIX C: EVALUATION OF COHERENCE PARAMETERS

In fact, if the Fourier-transformed intensities $\hat{I}^{\text{pc}}(\mathbf{k}, z)$ and $\hat{I}^{\text{fc}}(\mathbf{k}, z)$ were known, the modulus of the $g_S(\mathbf{k}, z)$ function could be evaluated as

$$|g_S(\mathbf{k}, z)| = \frac{|\hat{I}^{\text{pc}}(\mathbf{k}, z)|}{|\hat{I}^{\text{fc}}(\mathbf{k}, z)|}. \quad (\text{C1})$$

Let us assume that the recovered intensity profiles $|E(\boldsymbol{\rho}, z_n)|^2$, generated by the PHARE code, represent a fully coherent case of the studied beam $I^{\text{fc}}(\boldsymbol{\rho}, z_n)$. Furthermore, provided that the measured intensity profiles $|E^M(\boldsymbol{\rho}, z_n)|^2$, obtained by means of PMMA desorption imprints, depict the actual partially coherent state of the studied beam $I^{\text{pc}}(\boldsymbol{\rho}, z_n)$, we can claim that

$$|g_S(\mathbf{k}, z_n)| = \frac{|\mathcal{F}[|E^M(\boldsymbol{\rho}, z_n)|^2](\mathbf{k})|}{|\mathcal{F}[|E(\boldsymbol{\rho}, z_n)|^2](\mathbf{k})|}. \quad (\text{C2})$$

Here the operator $\mathcal{F}[\cdot](\mathbf{k})$ stands for the Fourier transform.

Such an analysis may seem straightforward; however, severe numerical issues arise when we attempt to express $|g_S(\mathbf{k}, z_n)|$ by imposing a simple division. Therefore, Taylor expansion is used in order to overcome problems connected with small numbers in the denominator. For the purposes of calculations, all the functions are represented as finite two-dimensional matrices. It can be proven that “element-by-element” inversion of a matrix \mathbf{A} , i.e., $B_{ij} = 1/A_{ij}$, can be conveniently expressed as

$$B_{ij} = \frac{1}{A_{ij}} \cong \frac{1}{A_{\max}} \sum_{k=0}^N \left(1 - \frac{A_{ij}}{A_{\max}}\right)^k, \quad (\text{C3})$$

provided that all matrix elements are positive ($A_{ij} \geq 0$ for all indices i and j). Here A_{\max} is the maximum matrix element, and N is the maximum order of expansion.

By expanding the denominator in Eq. (C2) to an appropriate order (in our case, $N = 40$), the modulus of the $g_S(\mathbf{k}, z_n)$ function can be determined to a reasonable accuracy. However, the presence of nonphysical features and artifacts of the aforementioned mathematical approach cannot be entirely excluded. Hence, in order to model the coherence correctly, an astigmatic Gaussian Schell model is used in the following factorized form:

$$\begin{aligned} &g(\boldsymbol{\rho}'_1 - \boldsymbol{\rho}'_2; z_{Sx}, z_{Sy}) \\ &= \exp\left[-\frac{(x'_1 - x'_2)^2}{2\sigma_{Sx}^2}\right] \exp\left[-\frac{(y'_1 - y'_2)^2}{2\sigma_{Sy}^2}\right], \end{aligned} \quad (\text{C4})$$

where σ_{Sx} and σ_{Sy} represent the coherence widths at the positions z_{Sx} and z_{Sy} of the respective horizontal (x) and

vertical (y) Schell-model sources. The $g_S(\mathbf{k}, z)$ function then reads

$$g_S(\mathbf{k}, z) = \exp\left[-\frac{(z - z_{Sx})^2}{2k^2\sigma_{Sx}^2}\kappa_x^2 - \frac{(z - z_{Sy})^2}{2k^2\sigma_{Sy}^2}\kappa_y^2\right]. \quad (\text{C5})$$

In order to obtain the coherence parameters σ_{Sx} , σ_{Sy} , z_{Sx} , and z_{Sy} , the above presented model function is to be fitted to the coherence data retrieved by means of Eq. (C2) with the aid of Eq. (C3). The fitting is done globally, i.e., simultaneously to all data at all measurement positions z_n .

One of the most important quantities enumerating the “quality” of transverse coherence is the so-called degree of transverse coherence which is supposed to be invariant for paraxial optical beams propagating in free space. In the simplest Gaussian Schell model approach (a Gaussian beam with a Gaussian complex degree of coherence), the degree of transverse coherence reads [45]

$$\xi = \frac{\sigma_S/\sigma}{\sqrt{4 + \sigma_S^2/\sigma^2}}, \quad (\text{C6})$$

where σ_S is the aforementioned transverse coherence width and σ is the beam width in the same transverse direction. Both values are measured in terms of the central second-order statistical moment (SCM) at the position of the secondary Schell-model source. The degree of coherence ranges from 0 to 1. Boundaries of this interval represent hardly achievable incoherent and fully coherent states of the wave field, respectively, whereas intermediate values stand for physically common partially coherent states.

Once a fully coherent wave field (a self-consistent output of the phase-retrieval algorithm) and coherence parameters are known, propagation of the partially coherent beam to an arbitrary z position can be done numerically with use of Eqs. (B2), (B3), and (C5). However, it is not necessary to solve the integral in Eq. (B3), since the propagated mutual optical intensity represents a fully coherent wave field and thus can be factorized as a product of the electrical field and its complex conjugate. Instead of Eq. (B3), the Fresnel diffraction integral, e.g., in the form of Eq. (1), can be used to propagate the fully coherent electrical wave field, and $\hat{I}^{\text{fc}}(\mathbf{k}, z)$ can be simply calculated as the Fourier transform of its squared modulus.

x-ray physics: Photon properties, beam transport system and applications, *New J. Phys.* **12**, 075002 (2009).

- [4] P. Emma *et al.*, First lasing and operation of an ångström-wavelength free-electron laser, *Nat. Photonics* **4**, 641 (2010).
- [5] T. Ishikawa *et al.*, A compact x-ray free-electron laser emitting in the sub-ångström region, *Nat. Photonics* **6**, 540 (2012).
- [6] A. J. Nelson *et al.*, Soft x-ray free electron laser microfocus for exploring matter under extreme conditions, *Opt. Express* **17**, 18271 (2009).
- [7] C. David, S. Gorelick, S. Rutishauser, J. Krzywinski, J. Vila-Comamala, V. A. Guzenko, O. Bunk, E. Farm, M. Ritala, M. Cammarata, D. M. Fritz, R. Barrett, L. Samoylova, J. Gruenert, and H. Sinn, Nanofocusing of hard x-ray free electron laser pulses using diamond based Fresnel zone plates, *Sci. Rep.* **1**, 57 (2011).
- [8] S. Le Pape, P. Zeitoun, M. Idir, P. Dhez, J. J. Rocca, and M. Francois, Electromagnetic-Field Distribution Measurements in the Soft X-Ray Range: Full Characterization of a Soft X-Ray Laser Beam, *Phys. Rev. Lett.* **88**, 183901 (2002).
- [9] B. Floeter, P. Juranic, S. Kapitzi, B. Keitel, K. Mann, E. Ploenjes, B. Schaefer, and K. Tiedtke, EUV Hartmann sensor for wavefront measurements at the Free-electron LASer in Hamburg, *New J. Phys.* **12**, 083015 (2010).
- [10] H. M. Quiney, A. G. Peele, Z. Cai, D. Paterson, and K. A. Nugent, Diffractive imaging of highly focused x-ray fields, *Nat. Phys.* **2**, 101 (2006).
- [11] H. Yumoto, H. Mimura, T. Koyama, S. Matsuyama, K. Tono, T. Togashi, Y. Inubushi, T. Sato, T. Tanaka, T. Kimura, H. Yokoyama, J. Kim, Y. Sano, Y. Hachisu, M. Yabashi, H. Ohashi, H. Ohmori, T. Ishikawa, and K. Yamauchi, Focusing of x-ray free-electron laser pulses with reflective optics, *Nat. Photonics* **7**, 43 (2013).
- [12] A. Schropp, R. Hoppe, V. Meier, J. Patommel, F. Seiboth, H. J. Lee, B. Nagler, E. C. Galtier, B. Arnold, U. Zastra, J. B. Hastings, D. Nilsson, F. Uhlen, U. Vogt, H. M. Hertz, and C. G. Schroer, Full spatial characterization of a nano-focused x-ray free-electron laser beam by ptychographic imaging, *Sci. Rep.* **3**, 1633 (2013).
- [13] J. Chalupský *et al.*, Characteristics of focused soft x-ray free-electron laser beam determined by ablation of organic molecular solids, *Opt. Express* **15**, 6036 (2007).
- [14] J. Chalupský, J. Krzywinski, L. Juha, V. Hájková, J. Cihelka, T. Burian, L. Vyšín, J. Gaudin, A. Gleeson, M. Jurek, A. R. Khorsand, D. Klinger, H. Wabnitz, R. Sobierajski, M. Störmer, K. Tiedtke, and S. Toleikis, Spot size characterization of focused non-Gaussian x-ray laser beams, *Opt. Express* **18**, 27836 (2010).
- [15] J. Chalupsky, P. Bohacek, V. Hajkova, S. P. Hau-Riege, P. A. Heimann, L. Juha, J. Krzywinski, M. Messerschmidt, S. P. Moeller, B. Nagler, M. Rowen, W. F. Schlotter, M. L. Swiggers, and J. J. Turner, Comparing different approaches to characterization of focused x-ray laser beams, *Nucl. Instrum. Methods Phys. Res., Sect. A* **631**, 130 (2011).
- [16] J. Chalupský, T. Burian, V. Hájková, L. Juha, T. Polcar, J. Gaudin, M. Nagasono, R. Sobierajski, M. Yabashi, and J. Krzywinski, Fluence scan: An unexplored property of a laser beam, *Opt. Express* **21**, 26363 (2013).
- [17] N. Gerasimova, S. Dziarzhyski, H. Weigelt, J. Chalupsky, V. Hajkova, L. Vysin, and L. Juha, In situ focus characterization

- [1] V. Ayvazyan *et al.*, Generation of GW Radiation Pulses from a VUV Free-Electron Laser Operating in the Femto-second Regime, *Phys. Rev. Lett.* **88**, 104802 (2002).
- [2] T. Shintake *et al.*, A compact free-electron laser for generating coherent radiation in the extreme ultraviolet region, *Nat. Photonics* **2**, 555 (2008).
- [3] E. Allaria, C. Callegari, D. Cocco, W. M. Fawley, M. Kiskinova, C. Masciovecchio, and F. Parmigiani, The FERMI@Elettra free-electron-laser source for coherent

- by ablation technique to enable optics alignment at an XUV FEL source, *Rev. Sci. Instrum.* **84**, 065104 (2013).
- [18] B. Nagler *et al.*, Turning solid aluminium transparent by intense soft X-ray photoionization, *Nat. Phys.* **5**, 693 (2009).
- [19] S. M. Vinko *et al.*, Electronic Structure of an XUV Photo-generated Solid-Density Aluminum Plasma, *Phys. Rev. Lett.* **104**, 225001 (2010).
- [20] E. Galtier, F. B. Rosmej, T. Dzelzainis, D. Riley, F. Y. Khattak, P. Heimann, R. W. Lee, A. J. Nelson, S. M. Vinko, T. Whitcher, J. S. Wark, T. Tschentscher, S. Toleikis, R. R. Faeustlin, R. Sobierajski, M. Jurek, L. Juha, J. Chalupsky, V. Hajkova, M. Kozlova, J. Krzywinski, and B. Nagler, Decay of Crystalline Order and Equilibration during the Solid-to-Plasma Transition Induced by 20-fs Microfocused 92-eV Free-Electron-Laser Pulses, *Phys. Rev. Lett.* **106**, 164801 (2011).
- [21] S. M. Vinko *et al.*, Creation and diagnosis of a solid-density plasma with an x-ray free-electron laser, *Nature (London)* **482**, 59 (2012).
- [22] O. Ciricosta *et al.*, Direct Measurements of the Ionization Potential Depression in a Dense Plasma, *Phys. Rev. Lett.* **109**, 065002 (2012).
- [23] J. M. Liu, Simple technique for measurements of pulsed Gaussian-beam spot sizes, *Opt. Lett.* **7**, 196 (1982).
- [24] A. Aquila, C. Ozkan, R. Sobierajski, V. Hajkova, T. Burian, J. Chalupsky, L. Juha, M. Stoermer, H. Ohashi, T. Koyama, K. Tono, Y. Inubushi, M. Yabashi, H. Sinn, T. Tschentscher, A. P. Mancuso, and J. Gaudin, Results from single shot grazing incidence hard x-ray damage measurements conducted at the SACLA FEL, *Proc. SPIE Int. Soc. Opt. Eng.* **8777**, 87770H (2013).
- [25] L. Raimondi, C. Svetina, N. Mahne, D. Cocco, F. Capotondi, E. Pedersoli, M. Manfredda, M. Kiskinova, B. Keitel, G. Brenner, E. Ploenjes, T. Mey, K. Mann, and M. Zangrando, Status of the K-B bendable optics at FERMI@Elettra FEL, *Proc. SPIE Int. Soc. Opt. Eng.* **9208**, 920804 (2014).
- [26] A. F. G. Leontowich, A. Aquila, F. Stellato, R. Bean, H. Fleckenstein, M. Prasciolu, M. Liang, D. P. DePonte, A. Barty, F. Wang, J. Andreasson, J. Hajdu, H. N. Chapman, and S. Bajt, Characterizing the focus of a multilayer coated off-axis parabola for FLASH beam at $\lambda = 4.3$ nm, *Proc. SPIE Int. Soc. Opt. Eng.* **8777**, 87770T (2013).
- [27] A. Singer, F. Sorgenfrei, A. P. Mancuso, N. Gerasimova, O. M. Yefanov, J. Gulden, T. Gorniak, T. Senkbeil, A. Sakdinawat, Y. Liu, D. Attwood, S. Dziarzhytski, D. D. Mai, R. Treusch, E. Weckert, T. Salditt, A. Rosenhahn, W. Wurth, and I. A. Vartanyants, Spatial and temporal coherence properties of single free-electron laser pulses, *Opt. Express* **20**, 17480 (2012).
- [28] Y. Qin, T. Nakajima, H. Zen, X. Wang, T. Kii, and H. Ohgaki, Characterization of non-Gaussian mid-infrared free-electron laser beams by the knife-edge method, *Infrared Phys. Technol.* **66**, 146 (2014).
- [29] J. Chalupsky *et al.*, Non-thermal desorption/ablation of molecular solids induced by ultra-short soft x-ray pulses, *Opt. Express* **17**, 208 (2009).
- [30] S. Lindaas, H. Howells, C. Jacobsen, and A. Kalinovsky, X-ray holographic microscopy by means of photoresist recording and atomic-force microscope readout, *J. Opt. Soc. Am. A* **13**, 1788 (1996).
- [31] P. Heimann, O. Krupin, W. F. Schlotter, J. Turner, J. Krzywinski, F. Sorgenfrei, M. Messerschmidt, D. Bernstein, J. Chalupsky, V. Hajkova, S. P. Hau-Riege, M. Holmes, L. Juha, N. Kelez, J. Luening, D. Nordlund, M. F. Perea, A. Scherz, R. Soufli, W. Wurth, and M. Rowen, Linac Coherent Light Source soft x-ray materials science instrument optical design and monochromator commissioning, *Rev. Sci. Instrum.* **82**, 093104 (2011).
- [32] W. F. Schlotter *et al.*, The soft x-ray instrument for materials studies at the linac coherent light source x-ray free-electron laser, *Rev. Sci. Instrum.* **83**, 043107 (2012).
- [33] K. Tiedtke *et al.*, Absolute pulse energy measurements of soft x-rays at the Linac Coherent Light Source, *Opt. Express* **22**, 21214 (2014).
- [34] R. Soufli, M. Fernandez-Perea, S. L. Baker, J. C. Robinson, E. M. Gullikson, P. Heimann, V. V. Yashchuk, W. R. McKinney, W. F. Schlotter, and M. Rowen, Development and calibration of mirrors and gratings for the soft x-ray materials science beamline at the Linac Coherent Light Source free-electron laser, *Appl. Opt.* **51**, 2118 (2012).
- [35] R. W. Gerchberg and W. O. Saxton, Practical algorithm for determination of phase from image and diffraction plane pictures, *Optik (Stuttgart)* **35**, 237 (1972).
- [36] J. R. Fienup, Phase retrieval algorithms: A comparison, *Appl. Opt.* **21**, 2758 (1982).
- [37] H. H. Bauschke, P. L. Combettes, and D. R. Luke, Phase retrieval, error reduction algorithm, and Fienup variants: A view from convex optimization, *J. Opt. Soc. Am. A* **19**, 1334 (2002).
- [38] L. J. Allen, W. McBride, N. L. O'Leary, and M. P. Oxley, Exit wave reconstruction at atomic resolution, *Ultramicroscopy* **100**, 91 (2004).
- [39] A. C. Schell, A technique for determination of radiation pattern of a partially coherent aperture, *IEEE Trans. Antennas Propag.* **15**, 187 (1967).
- [40] L. Mandel and E. Wolf, *Optical Coherence and Quantum Optics* (Cambridge University Press, Cambridge, England, 1995).
- [41] K. A. Nugent, Coherent methods in the x-ray sciences, *Adv. Phys.* **59**, 1 (2010).
- [42] G. Gbur and E. Wolf, The Rayleigh range of Gaussian Schell-model beams, *J. Mod. Opt.* **48**, 1735 (2001).
- [43] I. A. Vartanyants *et al.*, Coherence Properties of Individual Femtosecond Pulses of an X-Ray Free-Electron Laser, *Phys. Rev. Lett.* **107**, 144801 (2011).
- [44] P. Paakkonen, J. Turunen, P. Vahimaa, A. T. Friberg, and F. Wyrowski, Partially coherent Gaussian pulses, *Opt. Commun.* **204**, 53 (2002).
- [45] I. A. Vartanyants and A. Singer, Coherence properties of hard x-ray synchrotron sources and x-ray free-electron lasers, *New J. Phys.* **12**, 035004 (2010).